Editors' Suggestion | Featured in Physics

Topological Anderson Insulator in Disordered Photonic Crystals

Gui-Geng Liu,[1,2] Yihao Yang,[1,2,*] Xin Ren,[3] Haoran Xue,[1] Xiao Lin,[1] Yuan-Hang Hu,[3] Hong-xiang Sun,[4] Bo Peng,[3] Peiheng Zhou,[3,†] Yidong Chong,[1,2,‡] and Baile Zhang[1,2,§]

[1]*Division of Physics and Applied Physics, School of Physical and Mathematical Sciences, Nanyang Technological University, 21 Nanyang Link, Singapore 637371, Singapore*

[2]*Centre for Disruptive Photonic Technologies, The Photonics Institute, Nanyang Technological University, 50 Nanyang Avenue, Singapore 639798, Singapore*

[3]*National Engineering Research Center of Electromagnetic Radiation Control Materials, State Key Laboratory of Electronic Thin Film and Integrated Devices, University of Electronic Science and Technology of China, Chengdu 610054, China*

[4]*Research Center of Fluid Machinery Engineering and Technology, School of Physics and Electronic Engineering, Jiangsu University, Zhenjiang, China*

(Received 12 April 2020; revised 22 July 2020; accepted 17 August 2020; published 24 September 2020)

Recent studies have revealed the counterintuitive possibility that increasing disorder can turn a topologically trivial insulator into a nontrivial insulator, called a topological Anderson insulator (TAI). Here, we propose and experimentally demonstrate a photonic TAI in a two-dimensional disordered gyromagnetic photonic crystal in the microwave regime. We directly observe the disorder-induced topological phase transition from a trivial insulator to a TAI with robust chiral edge states. We also demonstrate topological heterostructures that host edge states at interfaces between domains with different disorder parameters.

DOI: 10.1103/PhysRevLett.125.133603

Photonic topological insulators (PTIs) are photonic crystals (PhCs) that possess a bulk photonic band gap and robust edge states tied to the topological features of the underlying photonic band structure [1]. They were first proposed by Haldane and Raghu [2,3], and experimentally demonstrated by Wang *et al.* [4] using a microwave-scale gyromagnetic PhC—a photonic analog of a Chern insulator. Subsequent developments in topological photonics [1] showed that many other photonic platforms can be used to realize PTIs, including coupled ring resonators [5–7] and waveguide arrays [8]. Applications for robust waveguiding [4,9,10], lasing [11–13], and on-chip communications [14] are being actively pursued.

The advent of topological photonics has drawn renewed attention to the role of disorder in PhCs, which has a long history stretching back to Johns' seminal study of localization in photonic structures [15]. Disordered PhCs have numerous interesting properties such as strong photon localization [16] and have found applications in random lasers [17,18], compact spectrometers [19], and photovoltaic devices [20]. In the context of topological photonics, topological edge states in PTIs are known to be robust against localization induced by weak local disorder [21], whereas sufficiently strong global disorder can induce mode localization [22,23]. More interesting still is the possibility that disorder, introduced into systems with broken time-reversal symmetry, can induce a transition between topologically trivial and nontrivial behaviors [24–27]. Such a disorder-induced topological insulator, or topological Anderson insulator (TAI), has a bulk gap spanned by protected edge states, like a Chern insulator, but in the absence of disorder it reverts to a conventional (topologically trivial) insulator with a bulk gap but no edge states. This phenomenon has recently been demonstrated in laser-written waveguide arrays [28] and cold atom lattices [29].

Here, we report on the experimental realization of a TAI in a microwave-scale PhC consisting of dielectric and gyromagnetic pillars arranged in a two-dimensional (2D) lattice. Disorder is introduced by randomly rotating the dielectric pillars in each unit cell, with the disorder strength parametrized by the maximum rotation angle. We use transmission spectrum measurements to determine the width of the bulk gap and the emergence of chiral topological edge states, and hence show that the dependence on disorder strength is consistent with theoretical predictions. Using field intensity mapping, we show that the topological edge states can bypass corners and defects of different shapes and sizes. Finally, we study disorder-induced topological heterostructures formed by domains of different disorder strengths, with chiral topological states flowing along the interfaces between different domains. This shows that topological edge states can be routed by modulating the amount of disorder present in a lattice.

Our experiments serve as a significant extension to the experimental studies previously reported in Refs. [28,29],

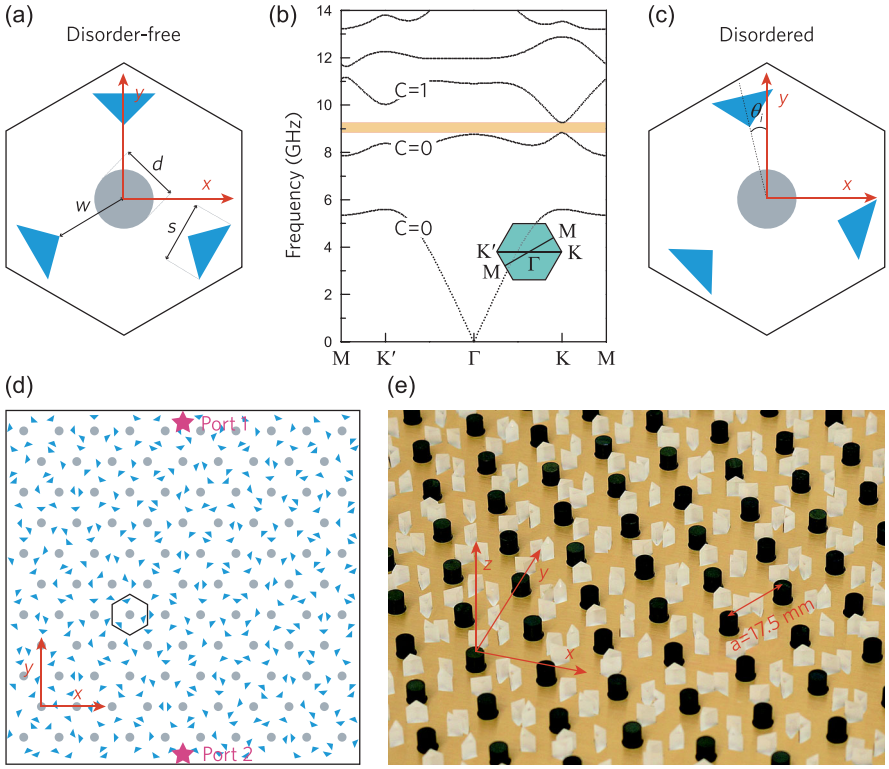

FIG. 1. Disordered gyromagnetic photonic crystal (PhC). (a) Unit cell of the disorder-free PhC ($\theta_d = 0°$), consisting of a central gyromagnetic cylinder (gray circle) surrounded by three dielectric right-triangular pillars (blue triangles). The diameter of the gyromagnetic cylinder $d = 4.4$ mm, the hypotenuse width of each right-triangular pillar is $s = 5.5$ mm, and the distance between the center of the unit cell and the nearest triangular vertex is $w = 4.7$ mm. (b) Band structure of the disorder-free PhC. The Chern numbers of the lowest three bands are labeled. (c) Typical cell of a disordered PhC, with the three triangular pillars rotated by a random angle θ uniformly distributed between $-\theta_d/2$ and $\theta_d/2$. (d) Sample of a disordered PhC with $\theta_d = 90°$. The pink stars indicate source and detector dipole antennas for measuring the bulk and edge transmission spectra. (e) Photograph showing a portion of the sample in (d). The PhC is loaded into a parallel waveguide with a height of 4 mm (the top plate is removed in this photograph). The sample size is $L_x \times L_y = 10a \times 10a$, where $a = 17.5$ mm is the lattice constant of the initial PhC.

demonstrating a broader range of physical properties of TAIs. In Ref. [28], Stützer *et al.* realized a TAI using an array of helical optical waveguides, with disorder introduced by varying the refractive indices of the waveguides. Because of the nature of this experimental platform, which maps the evolution of waveguide modes to a time-dependent Schrödinger equation, evidence for TAI behavior was limited to mapping the field intensities produced by midgap emitters placed at the lattice boundary. By contrast, our present experiments reveal the full frequency spectra emitted by sources inside the lattice or along its boundary, allowing us to observe the extent of the bulk gap as well as the gapless and robust nature of the edge transmission. From these spectra, we are able to map out the disorder-induced topological transition—the closing of a trivial gap and reopening of a topologically nontrivial gap with increasing disorder strength. Meier *et al.* have also observed TAI behavior in a disordered lattice of cold atoms [29]. However, this was a one-dimensional lattice in which the topological states are localized at the lattice boundaries, and do not propagate; moreover, the spectrum was not observed in the experiment.

Figure 1(a) shows a schematic of the unit cell of the initial, disorder-free PhC. A gyromagnetic rod is surrounded by three dielectric right-triangular pillars. The unit cells are arranged in a 2D triangular lattice with lattice constant $a = 17.5$ mm. The PhC is placed in an air-loaded waveguide composed of two parallel copper plates and with a static magnetic field $B = 0.45$ T applied along the out-of-plane (z) axis. The band diagram and Chern numbers for the lowest three transverse-magnetic (TM) bands (for which the electric fields are parallel to z) are shown in Fig. 1(b). There is a complete band gap between the second and third bands which is topologically trivial (i.e., the Chern numbers of all bands below the band gap sum to zero), because the parity-symmetry breaking counteracts the effects of time-reversal symmetry breaking [30]. The gyrotropy in this system is local [31], as in previous experiments on gyromagnetic PhCs [4]; the effects of nonlocal gyrotropy [32,33] are negligible.

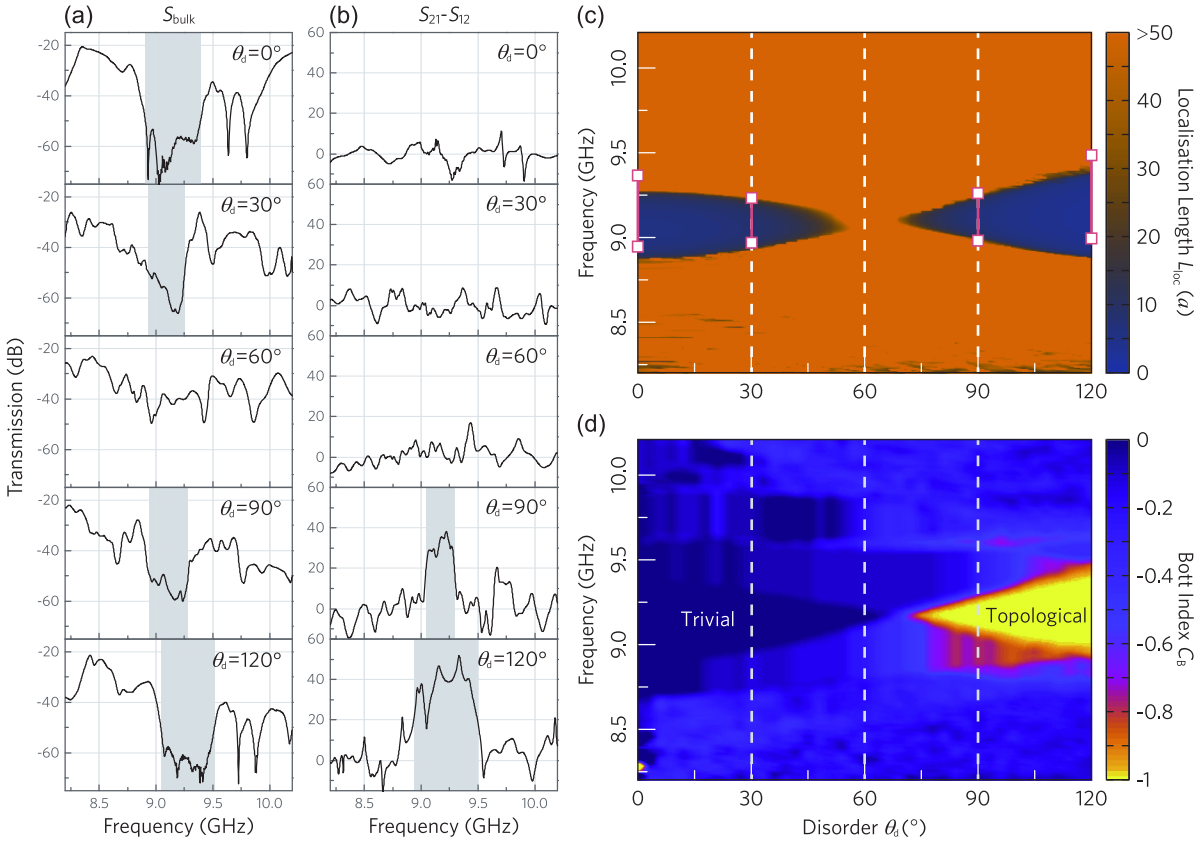

FIG. 2. Observation of disorder-induced topological phase transition. (a) Measured bulk transmission spectra. Gray regions indicate the measured bulk band gaps (defined by $S_{\text{bulk}} < -50$ dB), which are 8.90–9.40, 8.93–9.25, 8.95–9.28, and 9.04–9.51 GHz for $\theta_d = 0°$, 30°, 90°, and 120°, respectively. No band gap is observed for $\theta_d = 60°$. (b) The difference between the measured transmission spectra S_{21} and S_{12}. Gray regions represent regions with unidirectional edge transmission ($|S_{21} - S_{12}| > 20$ dB). No unidirectional edge transportation is observed for $\theta_d = 0°$, 30°, and 60°. (c) Simulated localization length L_{loc}. The band gap region ($L_{\text{loc}} < 5a$) is clearly distinguishable from in-band regions ($L_{\text{loc}} > 50a$). The pink lines with square ends show the measured gaps in (a). (d) Simulated Bott index C_B. With increasing disorder strength, the trivial band gap ($C_B = 0$) closes and reopens as a nontrivial band gap ($C_B = -1$).

This topologically trivial PhC can be driven into the topologically nontrivial regime by introducing disorder in the following manner: for each cell i, the three dielectric pillars are synchronously rotated around the center of the cell by a rotation angle θ_i, as shown in Fig. 1(c). We set $\theta_i = \theta_d R_i$, where θ_d is a constant that characterizes the disorder strength of the entire lattice and R_i is a random number that is drawn independently for each cell i and uniformly distributed between -0.5 and 0.5. As designed, the pillars cannot overlap regardless of the choice of R_i. Figures 1(d) and 1(e) show a typical disorder realization for $\theta_d = 90°$ [31].

We next perform bulk and edge transmission measurements on experimental samples with different values of θ_d. All samples have size $L_x \times L_y = 10a \times 10a$, as shown in Fig. 1(d) [31]. To measure the edge transmission, we cover the upper, right, and bottom boundaries of the sample with copper cladding, and cover the left boundary with microwave absorbers. The copper cladding serves as a perfect electric conductor (PEC) at microwave frequencies, equivalent to a photonic insulator with a trivial band gap [4,31]. The edge transmission S_{21}/S_{12} is measured with a source antenna placed at port 1/port 2 and a detector antenna at port 2/port 1. For the bulk transmission measurements, the experimental setup is almost identical except that all boundaries are covered with microwave absorbers.

Figures 2(a)–2(b) show the measured bulk and edge transmission spectra. In Fig. 2(a) the shaded regions indicate the measured bulk gaps (defined as frequency ranges where $S_{\text{bulk}} < -50$ dB), and in Fig. 2(b) the shaded regions indicate the frequency range over which edge states are observed (defined by $|S_{21} - S_{12}| > 20$ dB). As θ_d is increased from 0° to 60°, the width of the band gap decreases and finally disappears; meanwhile, the edge transmission in the gap region is low and there is negligible difference between forward and backward transmission. As we continue increasing θ_d, a bulk band gap reappears at $\theta_d = 90°$, and unidirectional edge transmission is observed ($|S_{21} - S_{12}| > 30$ dB). At $\theta_d = 120°$, the bulk band gap reaches its maximum width (>0.5 GHz). These measured bulk and edge transmission characteristics are explicit

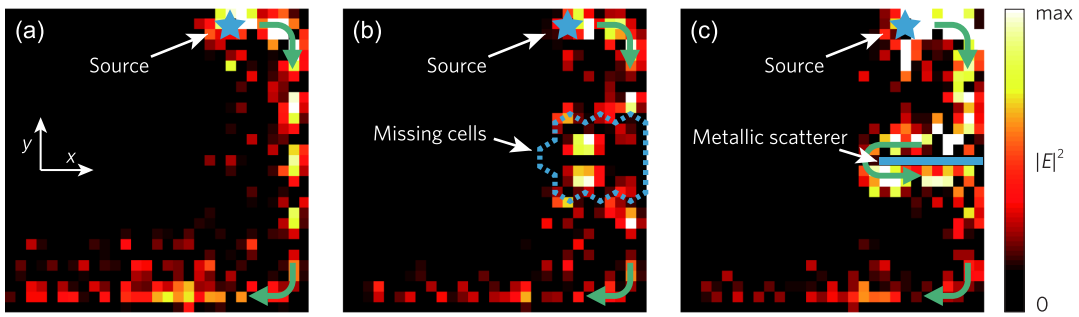

FIG. 3. Robustness of chiral edge states in disordered PhC-based TAIs. The TAIs have $\theta_d = 120°$ and measurements are performed at 9.2 GHz, near the middle of the band gap. The upper, right, and bottom boundaries of the sample have copper claddings, and the left boundary is covered with microwave absorbers. The colors show the measured distribution of $|E|^2$ excited by a dipole source (blue star). (a) Sample without any additional defects or obstacles. (b) Sample with a defect consisting of 9 unit cells removed in the region marked by blue dashes. (c) Sample with a large obstacle consisting of a copper bar (blue rectangle) of size 5 mm × 60 mm × 4 mm.

evidence of a disorder-driven transition from a topologically trivial to nontrivial phase.

To further quantify this topological transition, we use finite element simulations (COMSOL Multiphysics) to calculate the localization length L_{loc} in the disordered PhCs. The simulated samples have size $L_x \times L_y = 48a \times 18a$, with periodic boundary conditions on the upper and lower boundaries; the left and right boundaries are set as input and output ports. To improve the accuracy of L_{loc}, the size along the propagation direction (L_x) is set to be $48a$, larger than the transverse width (L_y). For each disorder configuration, the localization length is determined as $L_{\mathrm{loc}} = -L_x/\ln(S)$, where S is the total transmittance. The simulated results are averaged over 30 configurations for each value of θ_d. The resulting localization lengths are plotted in Fig. 2(c). For $\theta_d = 0°$, the extremely short localization length ($L_{\mathrm{loc}} < 5a$) in the 8.88–9.27 GHz range corresponds to the bulk band gap. Outside the band gap, we observe $L_{\mathrm{loc}} > 50a$ corresponding to transmission via bulk states. Upon increasing θ_d, the bulk band gap evidently closes around $\theta_d = 60°$, then reopens. The critical value of θ_d is dependent on various system parameters, such as the initial position of pillars [31]. Note that the periodic boundary conditions used in these simulations forbid the existence of edge states, so the resulting localization lengths do not distinguish between topologically nontrivial and trivial band gaps.

To characterize topological properties of a disordered system, topological invariants such as the Bott index [34] and generalized Chern number [35,36] have been proposed. Here, we use the Bott index (C_B) [34] to analyze simulations of disordered PhC slabs of size $L_x \times L_y = 18a \times 18a$, with periodic boundary conditions imposed in the two spatial directions. To calculate C_B at a specific disorder strength θ_d and frequency f, we first compute all eigenstates with eigenfrequencies below f. Then we calculate two unitary matrices, $U_X = \exp(i2\pi X/L_x)$ and $U_Y = \exp(i2\pi Y/L_y)$, where X and Y are diagonal matrices with x and y coordinates as diagonal elements, respectively. The Bott index C_B is then found by averaging $(1/2\pi)\mathrm{Im}\{\mathrm{tr}[\ln(\tilde{U}_Y\tilde{U}_X\tilde{U}_Y^{\dagger}\tilde{U}_X^{\dagger})]\}$ over a large number of different disorder configurations [26,34]. Here, $\tilde{U}_X$ and $\tilde{U}_Y$ are commutative block matrices given by $\tilde{U}_X = PU_XP$ and $\tilde{U}_Y = PU_YP$, and P is the projection operator to all states below f [31]. Figure 2(d) shows the Bott index averaged over 30 configurations for each value of θ_d. We find that the band gap for $\theta_d < 60°$ is topologically trivial ($C_B = 0$), and the band gap for $\theta_d > 60°$ is nontrivial ($C_B = -1$).

It is notable that the topologically nontrivial band gap occurs at *large* disorder strengths. Hence, this topological insulator phase is a photonic TAI [26]. The TAI behavior can be understood intuitively as follows: in the disorder-free PhC, the effects of time-reversal-symmetry breaking (which would normally turn the PhC into a Chern insulator [4]) is overridden by the parity symmetry breaking caused by the dielectric pillars in each unit cell. When disorder is introduced into the rotation angle of the dielectric pillars, the effective parity breaking is weakened, allowing the Chern insulatorlike features to surface [31].

To directly visualize the chiral edge propagation, we map the field intensity point by point inside the sample. As shown in Fig. 3(a), when a source is placed along the sample boundary, the emitted fields are strongly confined to the sample edges, and can propagate clockwise across two 90° bends without significant losses. We then introduce a large defect (by removing several unit cells along the boundary) or scatterer (a metallic bar placed along the boundary). As shown in Figs. 3(c)–3(d), the waves bypass the defect and obstacle with negligible backscattering. Using simulations, we have verified that different disorder configurations, drawn independently with the same θ_d, exhibit similar field intensity patterns [31].

The TAI phenomenon provides an opportunity to use disorder as a novel degree of freedom for manipulating topological edge states. To illustrate this, we construct a heterostructure composed of two disordered PhC domains with different disorder strengths, as shown in

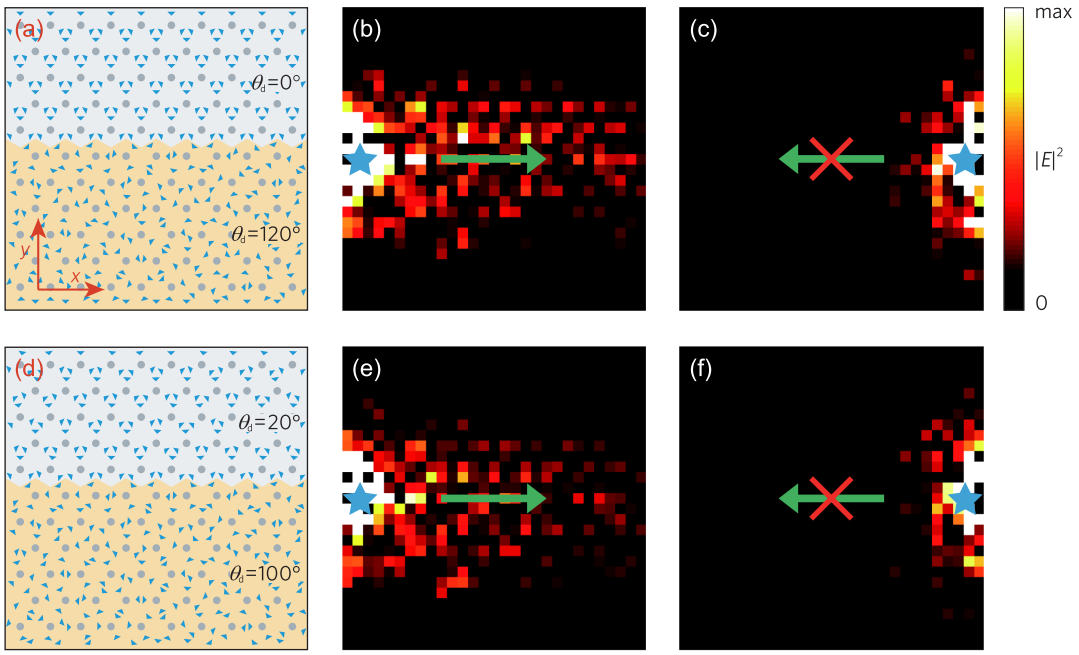

FIG. 4. Disorder-induced topological heterostructures. (a) Schematic of a heterostructure composed of a disorder-free PhC ($\theta_d = 0°$) and a TAI ($\theta_d = 120°$). (b)–(c) Measured field distributions ($|E|^2$) for the structure in (a), with source and probe antennas placed at opposite ends of the interface. (d) Schematic of a heterostructure composed of a disordered trivial PhC ($\theta_d = 20°$) and a TAI ($\theta_d = 100°$). (e)–(f) Measured field distributions ($|E|^2$) for the structure in (d), with source and detector antennas at opposite ends of the interface.

Figs. 4(a) and 4(d). The PhC domains in Fig. 4(a) have $\theta_d = 0°(C_B = 0)$ and $\theta_d = 120°(C_B = -1)$, and the domains in Fig. 4(d) have $\theta_d = 20°(C_B = 0)$ and $\theta_d = 100°(C_B = -1)$; all other parameters are kept the same. Hence, both cases feature a domain wall between a conventional disordered insulator and a TAI, established purely by a spatially inhomogeneous distribution of disorder strength. We place a source antenna near one end of the interface and scan the detector antenna through the whole sample. The resulting field distributions, shown in Figs. 4(b)–4(c) and 4(e)–4(f), reveal waves can propagate in only one direction along the interface.

We have thus experimentally demonstrated a TAI in a 2D disordered gyromagnetic PhC. The disorder drives a trivial disordered PhC into a topological one, as verified by transmission measurements and field mapping experiments, as well as localization length and Bott index calculations derived from finite-element simulations. We have used field mapping to demonstrate the robustness of the chiral edge states in the presence of sharp bends, defects, and obstacles. Moreover, we have demonstrated disorder-induced topological heterostructures, which use spatial variations in the disorder strength to establish interfaces hosting topological edge states—a new and interesting way to modulate electromagnetic waves. The ease with which disorder can be customized in this photonic platform opens many possibilities for further studies, such as disorder-induced three-dimensional topological phase transitions [27], disordered photonic circuits [37], disorder-induced nonlinear response [38,39], and disordered topological lasers [11–13].

The authors thank Professor Terry Loring for helpful discussions. This work was sponsored by the Singapore Ministry of Education under Grants No. MOE2016-T3-1-006, No. MOE2018-T2-1-022 (S), Tier 1 RG187/18, and by National Key Research and Development Program of China under Grant No. 2016YFB1200100, and by the program of China Scholarships Council under Grant No. 201806075001, and by the National Natural Science Foundation of China under Grant No. 11774137, and by State Key Laboratory of Acoustics, Chinese Academy of Science under Grant No. SKLA202016.

*yang.yihao@ntu.edu.sg
†phzhou@uestc.edu.cn
‡yidong@ntu.edu.sg
§blzhang@ntu.edu.sg

[1] T. Ozawa *et al.* Topological photonics, Rev. Mod. Phys. **91**, 015006 (2019).
[2] F. D. M. Haldane and S. Raghu, Possible Realization of Directional Optical Waveguides in Photonic Crystals with Broken Time-Reversal Symmetry, Phys. Rev. Lett. **100**, 013904 (2008).

[3] S. Raghu and F. D. M. Haldane, Analogs of quantum-Hall-effect edge states in photonic crystals, Phys. Rev. A **78**, 033834 (2008).

[4] Z. Wang, Y. Chong, J. D. Joannopoulos, and M. Soljačić, Observation of unidirectional backscattering-immune topological electromagnetic states, Nature (London) **461**, 772 (2009).

[5] M. Hafezi, E. A. Demler, M. D. Lukin, and J. M. Taylor, Robust optical delay lines with topological protection, Nat. Phys. **7**, 907 (2011).

[6] G. Q. Liang and Y. D. Chong, Optical Resonator Analog of a Two-Dimensional Topological Insulator, Phys. Rev. Lett. **110**, 203904 (2013).

[7] M. Hafezi, S. Mittal, J. Fan, A. Migdall, and J. M. Taylor, Imaging topological edge states in silicon photonics, Nat. Photonics **7**, 1001 (2013).

[8] M. C. Rechtsman, J. M. Zeuner, Y. Plotnik, Y. Lumer, D. Podolsky, F. Dreisow, S. Nolte, M. Segev, and A. Szameit, Photonic Floquet topological insulators, Nature (London) **496**, 196 (2013).

[9] Y. Poo, R. X. Wu, Z. Lin, Y. Yang, and C. T. Chan, Experimental Realization of Self-Guiding Unidirectional Electromagnetic Edge States, Phys. Rev. Lett. **106**, 093903 (2011).

[10] M. I. Shalaev, W. Walasik, A. Tsukernik, Y. Xu, and N. M. Litchinitser, Robust topologically protected transport in photonic crystals at telecommunication wavelengths, Nat. Nanotechnol. **14**, 31 (2019).

[11] Y. Zeng *et al.* Electrically pumped topological laser with valley edge modes, Nature (London) **578**, 246 (2020).

[12] M. A. Bandres, S. Wittek, G. Harari, M. Parto, J. Ren, M. Segev, D. N. Christodoulides, and M. Khajavikhan, Topological insulator laser: Experiments, Science **359**, eaar4005 (2018).

[13] B. Bahari, A. Ndao, F. Vallini, A. E. Amili, Y. Fainman, and B. Kanté, Nonreciprocal lasing in topological cavities of arbitrary geometries, Science **358**, 636 (2017).

[14] Y. Yang, Y. Yamagami, X. Yu, P. Pitchappa, B. Zhang, M. Fujita, T. Nagatsuma, and R. Singh, Terahertz topological photonics for on-chip communication, Nat. Photonics **14**, 446 (2020).

[15] S. John, Electromagnetic Absorption in a Disordered Medium near a Photon Mobility Edge, Phys. Rev. Lett. **53**, 2169 (1984).

[16] J. Topolancik, B. Ilic, and F. Vollmer, Experimental Observation of Strong Photon Localization in Disordered Photonic Crystal Waveguides, Phys. Rev. Lett. **99**, 253901 (2007).

[17] M. Lee, J. Lee, S. Kim, S. Callard, C. Seassal, and H. Jeon, Anderson localizations and photonic band-tail states observed in compositionally disordered platform, Sci. Adv. **4**, e1602796 (2018).

[18] M. Lee, S. Callard, C. Seassal, and H. Jeon, Taming of random lasers, Nat. Photonics **13**, 445 (2019).

[19] B. Redding, S. F. Liew, R. Sarma, and H. Cao, Compact spectrometer based on a disordered photonic chip, Nat. Photonics **7**, 746 (2013).

[20] K. Vynck, M. Burresi, F. Riboli, and D. S. Wiersma, Photon management in two-dimensional disordered media, Nat. Mater. **11**, 1017 (2012).

[21] S. Mansha and Y. D. Chong, Robust edge states in amorphous gyromagnetic photonic lattices, Phys. Rev. B **96**, 121405 (2017).

[22] C. Liu, W. Gao, B. Yang, and S. Zhang, Disorder-Induced Topological State Transition in Photonic Metamaterials, Phys. Rev. Lett. **119**, 183901 (2017).

[23] P. Zhou, G. G. Liu, X. Ren, Y. Yang, H. Xue, L. Bi, L. Deng, Y. Chong, and B. Zhang, Amorphous photonic topological insulator, Light Sci. Appl. **9**, 133 (2020).

[24] J. Li, R. L. Chu, J. K. Jain, and S. Q. Shen, Topological Anderson Insulator, Phys. Rev. Lett. **102**, 136806 (2009).

[25] C. W. Groth, M. Wimmer, A. R. Akhmerov, J. Tworzydło, and C. W. J. Beenakker, Theory of the Topological Anderson Insulator, Phys. Rev. Lett. **103**, 196805 (2009).

[26] P. Titum, N. H. Lindner, M. C. Rechtsman, and G. Refael, Disorder-Induced Floquet Topological Insulators, Phys. Rev. Lett. **114**, 056801 (2015).

[27] H. M. Guo, G. Rosenberg, G. Refael, and M. Franz, Topological Anderson Insulator in Three Dimensions, Phys. Rev. Lett. **105**, 216601 (2010).

[28] S. Stützer, Y. Plotnik, Y. Lumer, P. Titum, N. H. Lindner, M. Segev, M. C. Rechtsman, and A. Szameit, Photonic topological Anderson insulators, Nature (London) **560**, 461 (2018).

[29] E. J. Meier, F. A. An, A. Dauphin, M. Maffei, P. Massignan, T. L. Hughes, and B. Gadway, Observation of the topological Anderson insulator in disordered atomic wires, Science **362**, 929 (2018).

[30] G. G. Liu, P. Zhou, Y. Yang, H. Xue, X. Ren, X. Lin, H. X. Sun, L. Bi, Y. Chong, and B. Zhang, Observation of an unpaired photonic Dirac point, Nat. Commun. **11**, 1873 (2020).

[31] See Supplemental Material at http://link.aps.org/supplemental/10.1103/PhysRevLett.125.133603 for the disorder configuration, the calculation of the Bott index, materials parameters and sample, chiral edges for different disorder configurations, phase transition point, TAI without local three-fold symmetry, and TAI with different boundary conditions.

[32] T. Van Mechelen and Z. Jacob, Quantum gyroelectric effect: Photon spin-1 quantization in continuum topological bosonic phases, Phys. Rev. A **98**, 023842 (2018).

[33] T. Van Mechelen and Z. Jacob, Unidirectional Maxwellian spin waves, Nanophotonics **8**, 1399 (2019).

[34] T. A. Loring and M. B. Hastings, Disordered topological insulators via C*-algebras, Europhys. Lett. **92**, 67004 (2010).

[35] A. Kitaev, Anyons in an exactly solved model and beyond, Ann. Phys. (Amsterdam) **321**, 2 (2006).

[36] N. P. Mitchell, L. M. Nash, D. Hexner, A. M. Turner, and W. T. Irvine, Amorphous topological insulators constructed from random point sets, Nat. Phys. **14**, 380 (2018).

[37] S. A. Skirlo, L. Lu, Y. Igarashi, Q. Yan, J. Joannopoulos, and M. Soljačić, Experimental Observation of Large Chern Numbers in Photonic Crystals, Phys. Rev. Lett. **115**, 253901 (2015).

[38] D. Smirnova1, D. Leykam, Y. Chong, and Y. Kivshar, Nonlinear topological photonics, Appl. Phys. Rev. **7**, 021306 (2020).

[39] Z. Z. Du, C. M. Wang, S. Li, H. Z. Lu, and X. C. Xie, Disorder-induced nonlinear Hall effect with time-reversal symmetry, Nat. Commun. **10**, 3047 (2019).